ACS APPLIED ENERGY MATERIALS

www.acsaem.org Article

Impact of the Gibbs–Thomson Effect on Lithium Solubility in Silver Used as an Alloy Lithium-Ion Battery Anode

John S. Corsi, Alexander K. Ng, Yewei Huang, and Eric Detsi*

Cite This: ACS Appl. Energy Mater. 2022, 5, 4547–4555 Read Online

ACCESS | Metrics & More | Article Recommendations | Supporting Information

ABSTRACT: Because the multiple phase transformations occurring in high-capacity Li-ion battery alloy anodes through solid-state diffusion are commonly hindered by the relatively sluggish Li-ion diffusion kinetics, nanostructured alloy anodes, such as nanoporous metals, have been widely used to reduce the diffusion distance and subsequently enhance the cycling performance. However, although the size-dependent Li solubility limits that dictate the (de)-lithiation-induced solid–solid phase transformations have been studied for various nanostructured intercalation cathode materials, investigations of this structure–property relationship for nanostructured alloy anodes are limited. In this work, bulk and nanoporous Ag anodes are investigated as model alloy anodes to determine the impact of the structure size on the (de)lithiation phase transformation pathways that occur during cycling. First, we simulated the open-circuit voltage (OCV) profile of a Ag anode using a CALPHAD-based approach, allowing the profile features to be linked to the underlying solid solution and reconstitution phase transformations expected to occur during cycling by the Ag–Li equilibrium binary phase diagram. By comparing experimental voltage profiles with this calculated OCV profile and the X-ray diffraction patterns of the lithiated anodes, we determine that Li-rich phases are formed near the surface of the Ag active material, and while the bulk alloy anode follows the phase transformation pathway expected by the simulated OCV profile, the nanoporous Ag anode pathway includes the formation of an unpredicted, metastable β solid solution phase. From this information, we develop models for the phase morphology of the lithiated bulk and nanoporous anodes. This work demonstrates that due to the Gibbs–Thomson effect, nanostructured alloy anodes can proceed through a different phase transformation pathway compared to their bulk counterparts, and, as a result, these materials may form nonequilibrium phases and complex phase morphologies that can contribute toward increased interfacial energy and stress that can result in early failure.

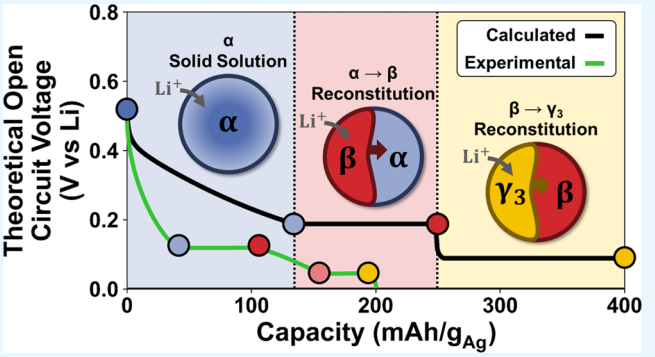

KEYWORDS: *Li-ion battery alloy anode, phase transformations, size-dependent solubility, Gibbs free energy, regular solution, nanoporous metals*

INTRODUCTION

High-capacity Li-ion battery (LIB) alloy anodes undergo large volume expansions during lithiation, which can result in pulverization and poor cycling performance.[1−4] Nanostructuring is a key strategy toward improving the poor cycling life of alloy anode active materials, where the reduced structure size is thought to improve the mechanical integrity during cycling.[2−6] While nanostructured alloy active materials, such as nanoporous metals, often have improved performance compared to their bulk counterparts, these materials still fail within less than a few hundred cycles, far below the cycle life needed for commercial viability.[7] To further improve the performance of nanoporous alloy anodes, a better understanding of the unique properties of these nanostructured alloy anode materials is needed.

One such property is the size-dependent Li solubility limits which dictate the (de)lithiation-induced solid–solid phase transformations that occur in high-capacity LIB alloy anodes. Decreasing the LIB electrode active material particle size, r, causes an increase in the overall Gibbs free energy of ΔG_{GT} known as the Gibbs–Thomson effect, shown in eq 1, where γ and V_m represent surface energy and molar volume, respectively.[8−10] For a given LIB electrode active material, A, this increase in Gibbs free energy alters the A–Li phase equilibria and shifts the Li solubility limits away from those predicted by an equilibrium binary phase diagram.[10] As a result, nanostructured electrode materials are expected to

Received: December 31, 2021
Accepted: March 29, 2022
Published: April 12, 2022

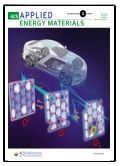

https://doi.org/10.1021/acsaem.1c04127
ACS Appl. Energy Mater. 2022, 5, 4547–4555

experience alternative phase transformation pathways compared to bulk materials during cycling.

$$\Delta G_{GT} = 2\gamma V_m/r \quad (1)$$

While size-dependent Li solubility limits have been widely studied for nanostructured insertion cathode materials such as Li_xFePO_4[11−15] and $Li_4Ti_5O_{12}$,[15−17] these structure−property relationships are less commonly investigated for nanostructured alloy anodes. In this work, the phase transformation pathways which occur in alloy anode materials will be comparatively investigated for bulk and nanoporous materials. Ag is used as a model anode for this purpose because the Ag−Li system features a variety of solid solution regions and two-phase regions that are present at room temperature.[18] Ag has been investigated as a LIB alloy anode in other work for its high theoretical capacity based on the formation of the γ_1-$Li_{12}Ag$ phase, low operating voltage, and high electrical conductivity.[1,19−22] Both bulk and nanoporous Ag (NP-Ag) anodes are investigated to determine the impact of morphology on the (de)lithiation phase transformation pathways which occur during cycling.

The voltage profile of a LIB half-cell can be used to monitor the underlying phase transformation pathways which occur in an electrode material during cycling. As shown in eq 2, the measured cell voltage (V) is equal to the theoretical open-circuit voltage (V_{OCV}), which depends on the underlying phase equilibria, minus the overpotential (η), which is a deviation from equilibrium conditions due to the summation of various kinetic effects. The shape of the OCV profile (i.e., plateau vs sloping) can be linked to the type of phase transformation occurring at a particular state of charge. Therefore, by comparing the experimental voltage profile with a known theoretical OCV curve to eliminate the influence of the overpotential, the underlying phase transformations taking place in experimental cells can be inferred.

$$V = V_{OCV} - \eta \quad (2)$$

In this work, Ag LIB anode OCV profiles are calculated using a CALPHAD-based approach.[23] The calculated OCV profile shape is linked to the underlying phase transformations expected by the Ag−Li phase diagram.[23] By comparing experimental voltage profiles of bulk and nanoporous Ag alloy anodes with the calculated Ag OCV profiles, the phase transformations that occur during cycling can be determined. Through this methodology, we are able to determine the Li solubility limit structure−property relationship for a Ag model alloy anode material and extend the resulting implications toward improving the performance of practical LIB alloy anode materials.

EXPERIMENTAL AND COMPUTATIONAL METHODS

Open-Circuit Voltage Modeling of the Ag−Li System. The OCV diagrams generated in this work were created using a CALPHAD-based approach described in detail in the Supporting Information. The FactSageEdu CALPHAD-based software is used to calculate the phase diagram and Gibbs free energy of the Ag−Li system as a function of Li composition, x, at room temperature.[24] From the Ag−Li Gibbs free energy, the composition-dependent Li chemical potential, $\mu_{Li}(x)$, can be calculated through eq 3,[8] which can be derived graphically from Figure S2 when the host material, A, is taken to be Ag. The cell V_{OCV} can then be calculated through eq 4,[25,26] where μ°_{Li}, z, and F represent the standard chemical potential of Li, Li-ion valency, and the Faraday constant, respectively. The Ag−Li system phase diagram, Gibbs free energy G, Li chemical potential μ_{Li}, and V_{OCV} are plotted on a common Li composition x-axis using Python code. This x-axis can be converted to cell capacity through a modified form of Faraday's law of electrolysis, as shown in eq 5, where q corresponds to the specific capacity and M corresponds to the atomic mass of Ag.

$$\mu_{Li}(x) = G(x) + \frac{dG(x)}{dx}(1-x) \quad (3)$$

$$V_{OCV}(x) = -(\mu_{Li}(x) - \mu^{\circ}_{Li})/zF \quad (4)$$

$$q = \frac{zF}{M}\cdot\frac{x}{1-x} \quad (5)$$

Fabrication of Nanoporous Ag. NP-Ag was fabricated through free corrosion dealloying of thermally processed Ag−Al parent alloys through a procedure previously reported in the literature.[27,28] First, a Ag−Al parent alloy of nominal composition Ag_5Al_{95} atom % (82.6 wt % Al) was synthesized by melting 4.97 g of Al shot (99.9% Alfa) and 1.067 g Ag shot (99.9% Alfa) within a graphite crucible using an induction furnace (MTI SP-15AB 15 kW induction heater). The equilibrium microstructure of this hypereutectic alloy material consists of a two-phase mixture of the δ intermediate phase and the (Al) terminal solid solution phase.[29] Dealloying a Ag−Al alloy with a two-phase microstructure results in a nonuniform nanoporous structure due to the different Al etching rates associated with each of the two phases.[27] To form uniform NP-Ag, the Ag−Al parent alloy two-phase microstructure was transformed into a single (Al) solid solution by annealing at 550 °C for 2 h in a tube furnace (OTF-1200X, MTI Corporation). The material was then immediately quenched in ice water to kinetically trap the nonequilibrium (Al) phase.[27]

The resulting parent alloy underwent free corrosion dealloying in 1 M HCl, where Al was selectively oxidized from the Ag−Al parent alloy, and the protons in the acid solution were reduced to evolve hydrogen gas. After 1.5 h, hydrogen evolution stopped, indicating that dealloying was complete. The sample was removed and washed in deionized water to prevent unnecessary chemical structural coarsening from occurring.[30] The resulting NP-Ag was found to consist of only ∼3 atom % Al after dealloying using energy-dispersive spectroscopy (EDS).

Bulk and Nanoporous Ag Half-Cell Assembly. A NP-Ag anode slurry was created, where the active material, the conductive material, and binder material constituted 50, 30, and 20 wt %, respectively. The conductive material consisted of a 1:1:1 mixture of C black (MTI TIMCAL Graphite & Super P Conductive Carbon Black) with zero-dimensional morphology, C nanofibers (100 nm D, 20−200 μm L, Sigma-Aldrich 719781) with one-dimensional morphology, and graphene nanoplatelets (330 m^2/g, Sigma-Aldrich 900394) with two-dimensional morphology. The binder material used was sodium carboxymethyl cellulose (CMC) ($M_w \sim 2\,50\,000$, Sigma-Aldrich 419311). The active and conductive materials were first ground together using a mortar and pestle before the CMC/H_2O binder solution was mixed in. The resulting slurries were cast on the rough side of Cu foil (9 μm thick, MTI EQ-bccf-9u) using a doctor blade. The slurries were dried in a vacuum oven (MTI EQ-DZF-6020-ETL) under vacuum for 12 h at 80 °C. The resulting electrode sheets were punched to form 1 cm diameter disks. Ag shot (1−5 mm 99.9%, Thermo Scientific 1143609) was rolled, polished, and punched to form disks of 1 cm^2 area and 70 μm thickness that served as the self-supported bulk Ag anode.

Using these two different anode materials, coin cells (MTI EQ-CR2032-CASE-LD) were assembled inside an Ar-filled glovebox. Whatman glass microfiber filters (Grade GF/C, Sigma-Aldrich WHA1822070) were used as the separators, Li foil (Guangdong New Energy Technology Co., Ltd.) as the counter electrodes, and 1 M $LiPF_6$ in a 1:1 ethylene carbonate (EC) and dimethyl carbonate solution (DMC) as the electrolyte. The cells were tested between 1 and 0.06 V vs Li/Li^+ using a Biologic VMP-300 potentiostat. The NP-Ag slurry electrodes were tested at a rate of C/5, while the free-

https://doi.org/10.1021/acsaem.1c04127
ACS Appl. Energy Mater. 2022, 5, 4547−4555

standing bulk Ag electrodes were tested at C/500, corresponding to current densities of ~50 and ~0.5 mA/g, respectively.

Materials Characterization. All electron microscopy was performed with a JEOL 7500F scanning electron microscope (SEM) equipped with an EDS detector. All X-ray diffraction (XRD) data were collected at a 0.02° step size and a 5°/min scanning speed using a Rigaku Miniflex powder diffractometer equipped with a Cu X-ray source and operated at 40 kV and 15 mA.

RESULTS AND DISCUSSION

Regular Solution Model of OCV Profile. The shape of the (dis)charge curve for a half-cell battery is often underappreciated as containing fundamental information pertaining to the phase transformation associated with the (dis)charging mechanism of a particular battery electrode. Huggins identifies two fundamental types of battery electrode reaction mechanisms that occur at near-equilibrium, each corresponding to a characteristic voltage curve shape: (1) an insertion-type lithiation reaction, where Li is inserted into vacant sites in the host crystal structure, as the potential decreases, and (2) a reconstitution-type lithiation reaction, where the addition of Li results in an increased amount of one host electrode phase and a decreased amount of the other host structure phase, as the potential remains constant.[31] Intercalation is a common type of insertion reaction in which Li is inserted between host material layers.[31] Huggins uses the Gibbs phase rule to establish a qualitative link between the underlying phase transformations taking place, as indicated by the system phase diagram and these two characteristic voltage curve shapes (i.e., sloping voltage curve vs voltage plateau).[31]

Here, a simple quantitative model − in which the anode material undergoing (de)lithiation, A, is treated as a regular solution of filled and vacant Li sites − is presented to build intuition for how the phase transformation behavior is linked to the shape of the voltage profile associated with Li storage in A.[32] An expression for the composition-dependent Gibbs free energy $G^{\mathrm{A}}(x)$ is given in eq 6, where x, Ω, R, and T represent Li concentration, interaction parameter, ideal gas constant, and temperature, respectively.[8] In this regular solution model, the Li concentration is represented by the fraction of filled Li sites in the host material A. The three terms in this equation represent the standard Gibbs free energy G^0, enthalpy of mixing $\Omega(x - x^2)$, and entropy of mixing $RT(x \ln x + (1 - x) \ln (1 - x))$, respectively. The interaction parameter, Ω, is proportional to the energy difference between mixing and segregating filled and unfilled sites. In this approach, the diffusional chemical potential shown in eq 7 is used, which, unlike the traditional chemical potential shown in eq 3, takes into account both the free energy change associated with adding Li to the electrode and the free energy change associated with accommodating the addition of these species.[32] This diffusional chemical potential can be substituted into eq 4 to yield the functional form of the V_{OCV} shown in eq 8. This expression for the OCV of a regular solution model electrode as a function of x has three terms: a standard potential term arising from the mechanical mixing term G^0 given by V^0, a linear regular solution term given by $\frac{\Omega}{zF}(2x - 1)$, and a logarithmic ideal solution term given by $\frac{RT}{zF}\ln\left(\frac{1-x}{x}\right)$.

$$G^{\mathrm{A}}(x) = G^0 + \Omega(x - x^2) + RT(x \ln x + (1 - x) \ln(1 - x)) \tag{6}$$

$$\mu^{\mathrm{A}}_{\mathrm{diff}}(\mathrm{x}) = \frac{\mathrm{d}}{\mathrm{d}x} G^{\mathrm{A}}(x) \tag{7}$$

$$V^{\mathrm{A}}_{\mathrm{OCV}}(x) = V^0 + \frac{\Omega}{zF}(2x - 1) + \frac{RT}{zF}\ln\left(\frac{1 - x}{x}\right) \tag{8}$$

Assuming standard conditions, the Gibbs free energy and OCV expression given in eqs 6 and 8, respectively, can be plotted as a function of x varying from zero to one for a range of interaction parameter values. For simplicity, both are plotted assuming standard Gibbs free energy and OCV values of zero. For values of the interaction parameter less than zero, the system prefers Li-vacancy mixing over Li-vacancy segregation. This results in a situation in which Li ions are inserted into vacant sites of the host crystal structure, which is referred to as an insertion reaction, as shown in Figure 1b. This will produce Gibbs free energy and OCV curves like those shown in Figure 1c,d, respectively. As the interaction parameter increases from zero, the Gibbs free energy curve becomes more and more depressed until, eventually, when the interaction parameter is greater than 2RT, two Gibbs free energy local minima are established, as shown in Figure 1f.[8,32] Since these minima share a common slope, the system would prefer to evolve along the dashed horizontal line during lithiation, maintaining a constant free energy rather than increasing the free energy of the system. Therefore, the common tangent line between these two points becomes the new Gibbs free energy of the system at these compositions, and, correspondingly, the OCV between these points is represented as a straight line, as shown in Figure 1g. This results in an entirely different reaction mechanism, referred to as a reconstitution reaction, as shown in Figure 1e, in which adding Li results in the transformation of a Li-poor phase, labeled α, into a Li-rich phase, labeled β.

In summary, the model above demonstrated that an insertion-type reaction involves a single-phase microstructure, where Li is inserted into the vacant sites in a host crystal structure, while a reconstitution-type reaction involves a two-phase microstructure, where the addition of Li results in the transformation of a Li-poor phase into a Li-rich phase. Insertion reactions result in a sloping voltage profile, while reconstitution reactions result in a voltage plateau. With this intuition established, we can transfer these reaction mechanisms to an OCV model with greater complexity.

Analysis of Ag Anode Open-Circuit Voltage Model. Figure 2a shows the Ag−Li phase diagram, where each single-phase region is shaded with a different color, and the two-phase regions are colored white. The phases present at room temperature are shown by the green line. The gray vertical lines indicate the room temperature solubility limits of the single-phase regions and the two-phase regions. The calculated Gibbs free energy, Li chemical potential, and OCV are shown in Figure 2b−d, respectively. By overlaying the solubility limits and single-phase region labels on these data, it is clear that the phase diagram has a direct impact on the behavior of the Gibbs free energy, Li chemical potential, and OCV curves. Single-phase regions are shown to correspond to sloping voltage data, while two-phase regions have constant voltage data. Due to overpotential effects, practical lithiation voltage data will be below the OCV in the region shaded green, and practical delithiation voltage data will be above the OCV in the region shaded red. Since the OCV falls to near-zero at around 70 atom % Li, only the region between 0 and 70 atom % Li will be considered in the following analysis. Thus, in this work, the

https://doi.org/10.1021/acsaem.1c04127
ACS Appl. Energy Mater. 2022, 5, 4547−4555

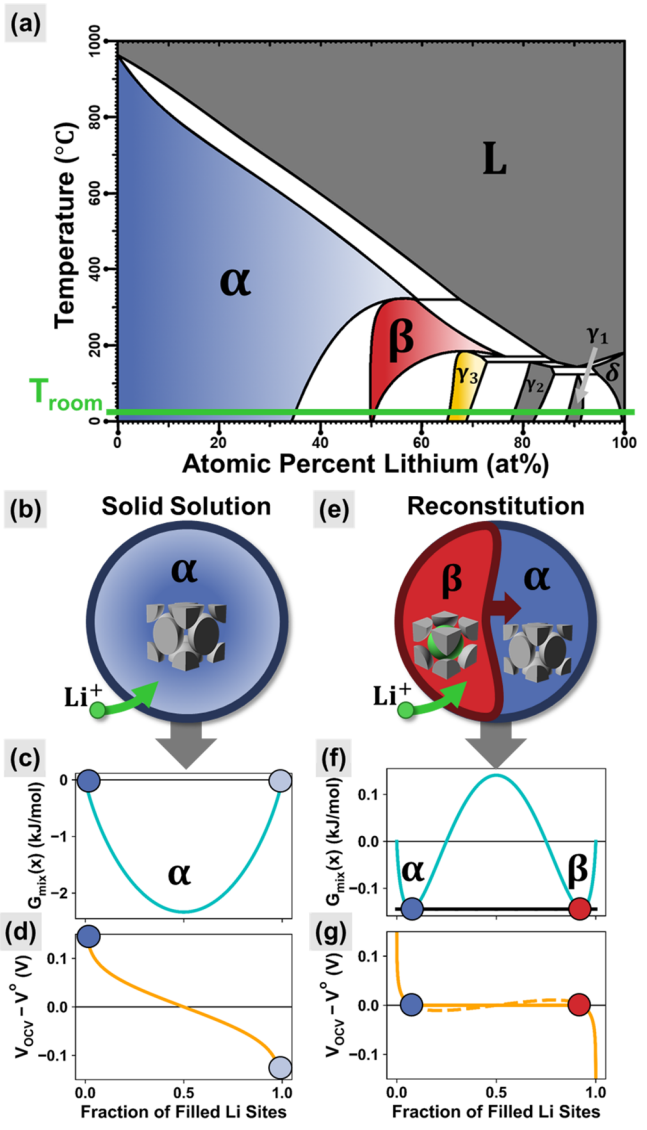

Figure 1. (a) Equilibrium binary phase diagram of Ag−Li system. Single-phase regions are labeled and in color, while two-phase regions are white. The figure was adapted with permission from Okamoto, H. Supplemental Literature Review of Binary Phase Diagrams: Ag−Li, Ag-Sn, Be-Pu, C-Mn, C-Si, Ca-Li, Cd-Pu, Cr-Ti, Cr-V, Cu-Li, La-Sc, and Li-Sc. *J. Phase Equilibria Diffus.* **2017**, 38 (1), 70−81.[18] Copyright 2017 Springer. Regular solution model of an electrode material, which results in either the insertion (b−d) or reconstitution (e−g) reaction behavior depending on the value of the interaction parameter. The insertion mechanism, shown schematically in (b), where Li is added to a host solid solution phase, has a Gibbs free energy of mixing with a single minimum shown in (c) and a sloping OCV profile shown in (d). The reconstitution mechanism, shown schematically in (e), where the addition of Li results in the conversion of Li-poor α to Li-rich β, has a Gibbs free energy of mixing with two minima shown in (f) and a flat OCV profile shown in (g).

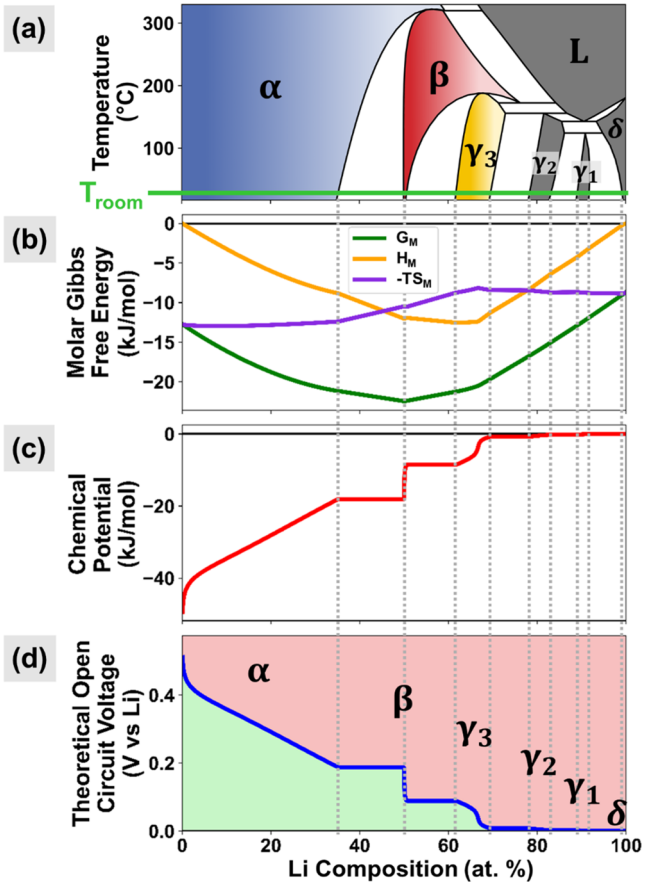

Figure 2. Simulation of (a) phase diagram, (b) Gibbs free energy, (c) Li chemical potential, and (d) theoretical OCV as a function of Li composition for the Ag−Li binary equilibrium system using a CALPHAD-based "FactSage methodology" described in the Supporting Information. In (b), G_M, H_M, and TS_M correspond to molar Gibbs free energy (green), molar enthalpy (orange), and the molar entropy times the operating temperature (purple).

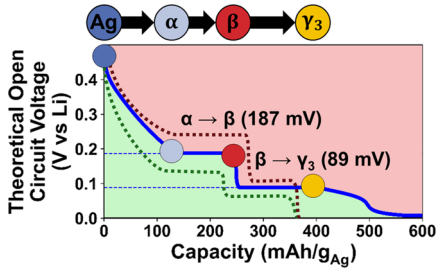

Figure 3. Calculated OCV diagram for a Ag LIB anode half-cell labeled with overlaid phase transformations. Compared to the equilibrium OCV curve (blue), practical lithiation voltage data will be lower in value (dotted green line), while practical delithiation voltage data will be higher (dotted red line).

maximum achievable practical capacity is expected to be 580 mAh/g, corresponding to the γ_3 phase solid solution reaction.

The OCV plot calculated in Figure 2d is replotted with the x-axis corresponding to capacity using eq 5, as shown in Figure 3, in which various equilibrium thermodynamic properties are calculated for the Ag−Li system as a function of Li composition. This diagram can be used to understand the insertion and reconstitution reactions that occur when cycling a Ag LIB anode. Note that experimental lithiation voltage data will be lower than the blue equilibrium curve due to overpotential, as shown by the dotted green line. Starting from pure Ag, Li will be inserted into the α solid solution as the voltage falls from 0.5 V vs Li/Li$^+$. Next, the α phase will be transformed to the β phase below 187 mV vs Li/Li$^+$. This is followed by the β phase transforming to form the γ_3 phase below 89 mV vs Li/Li$^+$. During delithiation, the phase transformations occur in the reverse order. Again, note that

https://doi.org/10.1021/acsaem.1c04127
ACS Appl. Energy Mater. 2022, 5, 4547−4555

experimental delithiation voltage data will be higher than the blue equilibrium curve due to overpotential, as shown by the dotted red line. To determine if real Ag anodes follow the phase transformation pathway suggested by the OCV simulation, bulk and nanoporous Ag anode half cells are cycled, and the resulting voltage profiles are analyzed.

Characterization and Cycling Performance of Bulk and Nanoporous Ag Anodes. The bulk and nanoporous Ag anodes explored in this work are characterized using scanning electron microscopy (SEM). Figure 4a,b shows the surface of the bulk Ag anode, indicating that no long-range microscale or nanoscale structure is present in this material. Figure 4c,d shows the surface of the dealloyed NP-Ag used in this work, indicating that the ligaments of the uniform nanoporous structure are ~50 nm thick.

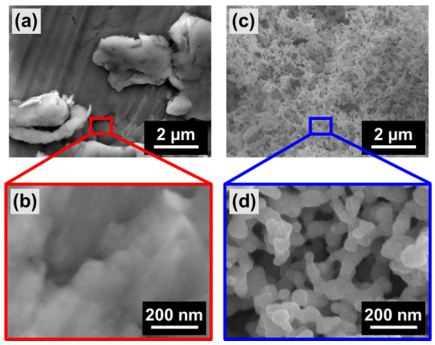

Figure 4. (a–b) Low- and high-magnification SEM images of pristine bulk Ag electrode. (c–d) Low- and high-magnification SEM images of pristine NP-Ag electrode.

Cyclic voltammetry (CV) was performed on each Ag morphology to determine the cycling voltage range. Figure 5a shows CV data in the voltage range from 60 mV to 0.8 V vs Li/Li$^+$. The specific current density (i.e., current normalized by the Ag mass) is used to demonstrate the relative activities of these two morphologies. Both CVs exhibit a major reduction peak below ~0.20 V vs Li/Li$^+$ associated with Li insertion in Ag, and a major oxidation peak at ~0.33 V vs Li/Li$^+$ associated with the removal of Li from Ag. The NP-Ag anode also shows CV oxidation peaks at 0.23, 0.175, and 0.1 V vs Li/Li$^+$ attributed to the delithiation of Li-rich phases. From these CVs, it is clear that the electrochemical activity of the NP-Ag electrode is much greater than the bulk Ag electrode, likely due to the enhanced surface area and reactivity of the nanoporous structure.

These anodes were further investigated with constant currents (galvanostatic tests) between 60 mV and 1 V vs Li/Li$^+$. In this voltage window, the maximum achievable capacity will be 580 mAh/g for the γ_3 phase, as defined earlier. The NP-Ag electrode cells were tested at C/5, while the bulk Ag cell was tested at C/500 since this was the highest current at which multiple cycles could be achieved. The cycling performance of these cells is shown in Figure 5b. Despite this low current, the bulk Ag cell achieves a maximum capacity of only ~1.5 mAh/g (corresponding to 0.3% of the maximum capacity of 580 mAh/g for the γ_3 phase) and, as shown by the enlarged plot in Figure S3, only survives 10 cycles. The NP-Ag electrode achieves a higher capacity of 200 mAh/g (corresponding to 34% of the maximum capacity of 580 mAh/g for the γ_3 phase), which decays over 30 cycles before reaching a plateau around ~175 mAh/g. Since the bulk and nanoporous Ag voltage profiles shown in Figure 5c,d, respectively, appear distinct, it is

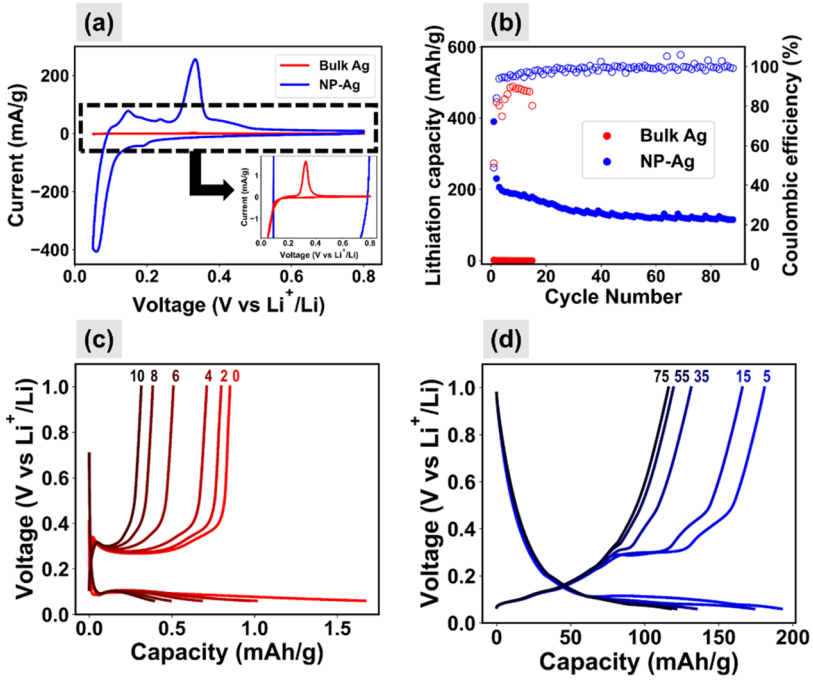

Figure 5. (a) Comparison of cyclic voltammograms of bulk Ag (red) and NP-Ag slurry (blue) electrodes vs Li in 1 M $LiClO_4$ performed at 50 μV/s between 60 mV to 0.8 V vs Li/Li$^+$. The fourth cycle is shown for each sample. The current is normalized by active material mass. (a, inset) Magnified region of voltammogram to show the bulk Ag signature. (b) Cycle life performance and Coulombic efficiency of bulk Ag cycled at C/500 (red) and NP-Ag cycled at C/5 (blue). Individual voltage profiles are shown for bulk Ag in (c) and NP-Ag slurry in (d), with cycle numbers labeled above the delithiation voltage profiles.

https://doi.org/10.1021/acsaem.1c04127
ACS Appl. Energy Mater. 2022, 5, 4547–4555

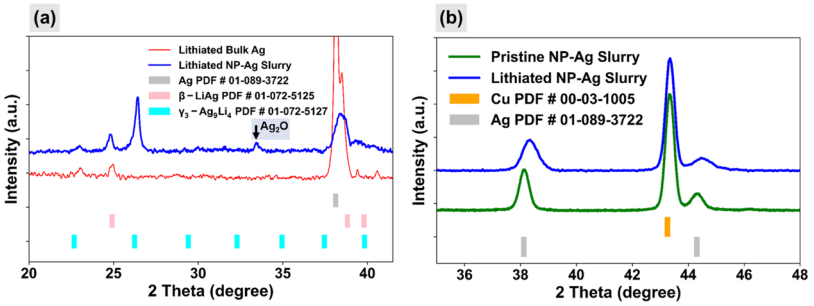

Figure 6. (a) XRD of lithiated bulk Ag (red) and NP-Ag slurry (blue) showing the presence of the Ag (gray, pink), and γ_3 (cyan) phases. (b) Comparison of Ag peaks of pristine (green) and lithiated NP-Ag slurry (blue).

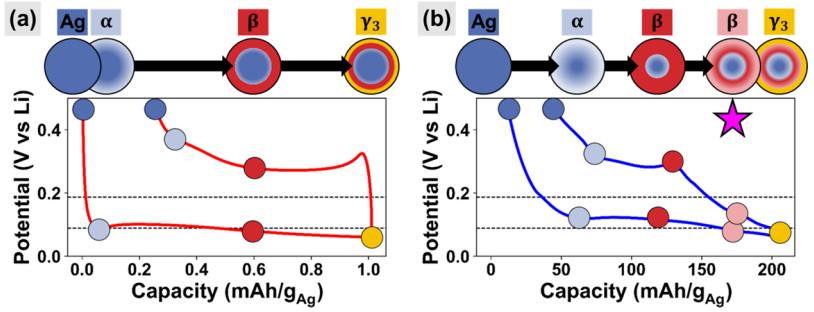

Figure 7. Voltage profiles with phase transformations labeled for (a) bulk and (b) nanoporous Ag anodes. For each electrode, the second cycle data is shown with the α to β and β to γ_3 reconstitution reaction plateaus (dashed black lines) from Figure 4 at 187 and 89 mV vs Li/Li$^+$, respectively. The nonequilibrium β solid solution phase is labeled with a pink star.

expected that the Ag morphology causes different phase transformation pathways to occur.

To determine the phases that form during lithiation, bulk and nanoporous Ag anodes were lithiated to 60 mV vs Li/Li$^+$, sealed in Kapton tape, and analyzed using X-ray diffraction (XRD), as shown in Figure 6a. Despite the low capacity achieved by these anodes, both are found to contain peaks corresponding to the Li-rich β and γ_3 phases. This indicates that the reactions are only occurring at the surfaces of the bulk and nanoporous materials. Both samples also show peaks corresponding to the Ag phase, indicating that the samples contain unreacted Ag cores. The Ag peaks of the lithiated NP-Ag sample are found to be significantly shifted compared to pristine NP-Ag, as shown in Figure 6b. This peak shifting is likely due to the insertion of Li into the α-Ag solid solution phase. The bulk Ag sample does not have significant peak shifting, indicating that significantly less Li is inserted into the α-Ag solid solution phase.

Phase Evolution Pathway for Bulk and Nanoporous Ag. To determine the phase evolution pathways through which the α, β, and γ_3 phases are formed during lithiation, the experimental voltage profiles are compared to the simulated OCV diagrams shown in Figure 3. From this analysis, the voltage profiles phase transformations are overlaid on the bulk and nanoporous Ag voltage profiles, as shown in Figure 7a,b, respectively.

As shown in Figure 7a, the bulk Ag anode is found to broadly match the phase transformation pathway predicted by the OCV simulation in Figure 3. Beginning with the pure Ag phase, the voltage decreases, indicating only a small amount of Li is inserted into the α solid solution phase. Next, there is a voltage plateau at 0.1 V vs Li/Li$^+$, corresponding to the α to β reconstitution phase transformation. The voltage then falls, reaching a second plateau at 65 mV vs Li/Li$^+$, corresponding to the β to γ_3 reconstitution phase transformation. During delithiation, the same phase transformation pathway is found to occur but in reverse order.

As shown in Figure 7b, lithiation of the nanoporous Ag anode is found to proceed through an alternative phase transformation pathway. Beginning with the pure Ag phase, the voltage has a sloping profile, indicating a significant amount of Li is inserted into the α solid solution phase. Next, there is a voltage plateau at 0.12 V vs Li/Li$^+$, corresponding to the α to β reconstitution phase transformation. Interestingly, instead of the plateau expected for the next reconstitution from Figure 3, a sloping region follows. Therefore, this region is determined to correspond to the insertion of Li in the β solid solution phase. Lastly, the voltage falls, reaching a second plateau at 75 mV vs Li/Li$^+$, corresponding to the β to γ_3 reconstitution phase transformation. During delithiation, the same phase transformation pathway is found to occur but in reverse. Importantly, a sloping region can be seen for the extraction of Li from the β solid solution phase, further supporting the presence of this alternative phase transformation pathway.

Comparing the phase transformation pathways of Figure 7b with Figure 3, the β phase is found to have an increased Li solubility for NP-Ag compared to the equilibrium calculations. Figure 8 shows schematically how the phase diagram, Gibbs free energy, and OCV of the NP-Ag anode differ from the calculated values in Figure 2. The β phase has increased Li solubility compared to the equilibrium Ag–Li phase diagram shown in Figure 1a. A schematic representation of the phase diagram for the NP-Ag anode updated with increased β phase Li solubility is shown in Figure 8a, where the dotted lines represent the equilibrium solubility limits. As a result of the high surface-to-volume ratio of the NP-Ag anode, the α free energy is increased due to the Gibbs–Thomson effect, as shown in eq 1. If the NP-Ag anode α phase were modeled as a

https://doi.org/10.1021/acsaem.1c04127
ACS Appl. Energy Mater. 2022, 5, 4547–4555

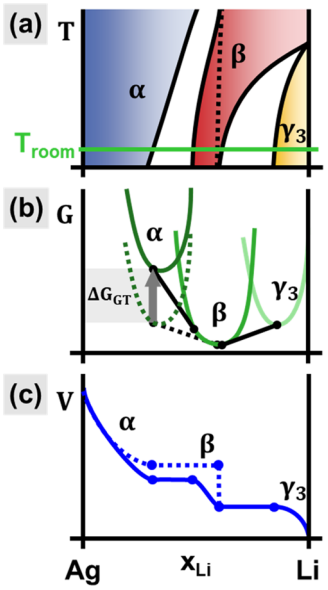

Figure 8. Schematic representation of the altered (a) phase diagram solubility limits, (b) Gibbs free energy, and (c) OCV profile of the NP-Ag anode. The equilibrium values are shown in dotted lines.

regular solution, its Gibbs free energy could be represented as a summation of eq 6, representing the traditional regular solution free energy, and eq 1, representing the additional free energy associated with the anode nanostructure, as a result of the Gibbs–Thomson effect. These new solubility limits change the free energy landscape, as shown in Figure 8b, which gives rise to a sloping OCV profile region corresponding to the insertion of Li into the β solid solution phase, as shown in Figure 8c.

From these data, we propose models for the phase morphologies of the bulk and nanoporous Ag anodes. The experimental capacities are found to be much lower than the theoretical capacities for each transformation, particularly in the case of bulk Ag. This indicates that these reactions are only taking place near the surface. In addition, XRD indicates the presence of α, β, and γ_3 phases. Therefore, we propose the Ag particles are composed of core–shell structures of these various phases. The bulk Ag phase morphology, shown in Figure 9a, has a nearly pure Ag α core with β and γ_3 shells near the surface. The NP-Ag phase morphology, shown in Figure 9b, has a Li-rich α solid solution core with a Li-rich β solid solution inner shell and a γ_3 outer shell.

CONCLUSIONS

In this work, we determine the phase transformation pathways of bulk and nanoporous Ag alloy anodes. First, we simulate the OCV profile of a Ag anode, and the curve features are linked to phase transformations occurring during cycling; sloping voltages are linked to single-phase solid solution insertion reactions, while voltage plateaus are linked to two-phase reconstitution reactions. Next, we cycle the bulk and nanoporous Ag anodes. XRD data is used to confirm that despite the low capacity achieved, Li-rich phases are formed. This indicates that the alloying reactions are taking place near the surface. From these data, the voltage profiles of these anodes are analyzed to determine which phase transformation pathways are occurring. While bulk alloy anodes follow the simulated OCV profile phase transformations, lithiation of NP-Ag results in the formation of a metastable β solid solution phase. From this information, models are developed for the anode phase morphology.

Therefore, this work demonstrates that nanostructured alloy anodes can proceed through a different phase transformation pathway compared to their bulk counterparts. The formation of nonequilibrium phases and complex phase morphologies likely contribute toward stress and interfacial energy that can lead to early cell failure. This investigation further reveals that although nanostructured alloy anodes theoretically allow for enhanced mechanical stability during cycling, other key properties such as Li solubility are impacted by nanostructuring and must be accounted for in designing commercially viable high-capacity alloy anodes. The approach developed in this work for the Ag model anode can also be used to study practical LIB alloy anodes such as Si, Al, Sn, and Sb, which have lower cost, higher capacity, and higher natural abundance than Ag. Understanding the impact of nanostructure on the phase equilibria for these systems may provide critical insight for the design of LIB alloy anode materials with enhanced performance.

ASSOCIATED CONTENT

Supporting Information

The Supporting Information is available free of charge at https://pubs.acs.org/doi/10.1021/acsaem.1c04127.

Discussion of CALPHAD-based approach to generate OCV diagrams; schematic overview of the process used to generate OCV diagrams; schematic of Gibbs free energy and Li chemical potential for the A–Li binary system as a function of Li atomic fraction; and enlarged view of bulk Ag cycle life performance and Coulombic efficiency (PDF)

AUTHOR INFORMATION

Corresponding Author

Eric Detsi – *Department of Materials Science & Engineering, University of Pennsylvania, Philadelphia, Pennsylvania 19104-6272, United States;* orcid.org/0000-0002-4009-7260; Email: detsi@seas.upenn.edu

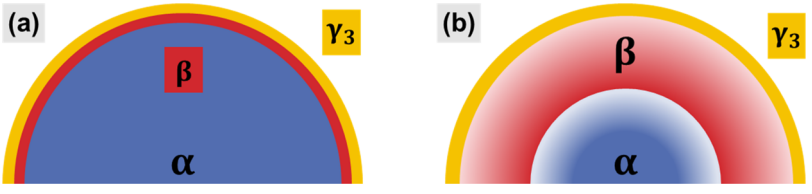

Figure 9. Schematic representation of the core–shell phase morphology of the lithiated (a) bulk Ag and (b) NP-Ag samples with the α (blue), β (red), and γ_3 (gold) phases labeled. Gradients indicate the presence of Ag–Li solid solutions.

https://doi.org/10.1021/acsaem.1c04127
ACS Appl. Energy Mater. 2022, 5, 4547–4555

Authors

John S. Corsi − *Department of Materials Science & Engineering, University of Pennsylvania, Philadelphia, Pennsylvania 19104-6272, United States;* orcid.org/0000-0001-5305-5521

Alexander K. Ng − *Department of Materials Science & Engineering, University of Pennsylvania, Philadelphia, Pennsylvania 19104-6272, United States;* orcid.org/0000-0002-3227-9582

Yewei Huang − *Department of Materials Science & Engineering, University of Pennsylvania, Philadelphia, Pennsylvania 19104-6272, United States;* orcid.org/0000-0001-6986-8068

Complete contact information is available at: https://pubs.acs.org/10.1021/acsaem.1c04127

Notes

The authors declare no competing financial interest.

■ ACKNOWLEDGMENTS

The authors are thankful to Penn Engineering and the Vagelos Institute for Energy Science and Technology (VIEST) for their financial support through the PI startup and the 2018 VIEST Fellowship to John S. Corsi. This work was performed in part at the Singh Center for Nanotechnology at the University of Pennsylvania, a member of the National Nanotechnology Coordinated Infrastructure (NNCI) network, which is supported by the National Science Foundation (Grant NNCI-1542153). The authors gratefully acknowledge use of facilities and instrumentation supported by NSF through the University of Pennsylvania Materials Research Science and Engineering Center (MRSEC) (DMR-1720530). The authors also acknowledge Prof. Eric A. Stach and Hyeongjun Koh for the characterization of lithiated Ag anodes with focused ion beam and transmission electron microscopy and Yihui Zhang for assistance in collecting SEM images.

■ REFERENCES

(1) Obrovac, M. N. N.; Chevrier, V. L. L. Alloy Negative Electrodes for Li-Ion Batteries. *Chem. Rev.* **2014**, *114*, 11444−11502.

(2) Li, H.; Shi, L.; Wang, Q.; Chen, L.; Huang, X. Nano-Alloy Anode for Lithium Ion Batteries. *Solid State Ionics* **2002**, *148*, 247−258.

(3) Goriparti, S.; Miele, E.; De Angelis, F.; Di Fabrizio, E.; Proietti Zaccaria, R.; Capiglia, C. Review on Recent Progress of Nano-structured Anode Materials for Li-Ion Batteries. *J. Power Sources* **2014**, *257*, 421−443.

(4) Mahmood, N.; Tang, T.; Hou, Y. Nanostructured Anode Materials for Lithium Ion Batteries: Progress, Challenge and Perspective. *Adv. Energy Mater.* **2016**, *6*, No. 1600374.

(5) Cho, J. Porous Si Anode Materials for Lithium Rechargeable Batteries. *J. Mater. Chem.* **2010**, *20*, 4009−4014.

(6) Cook, J. B.; Lin, T. C.; Detsi, E.; Weker, J. N.; Tolbert, S. H. Using X-Ray Microscopy To Understand How Nanoporous Materials Can Be Used To Reduce the Large Volume Change in Alloy Anodes. *Nano Lett.* **2017**, *17*, 870−877.

(7) Ding, Y.; Zhang, Z. *Nanoporous Metals for Advanced Energy Technologies*; Springer International Publishing: Cham, 2016.

(8) Porter, D. A.; Easterling, K. E.; Sherif, M. Y. *Phase Transformations in Metals and Alloys*, 3rd ed.; CRC Press, 2009.

(9) Perez, M. Gibbs-Thomson Effects in Phase Transformations. *Scr. Mater.* **2005**, *52*, 709−712.

(10) Weissmüller, J. Thermodynamics of Nanocrystalline Solids. In *Nanocrystalline Metals and Oxides*; Kluwer Academic Publishers: Boston, 2005; pp 1−39.

(11) Bai, P.; Cogswell, D. A.; Bazant, M. Z. Suppression of Phase Separation in $LiFePO_4$ Nanoparticles During Battery Discharge. *Nano Lett.* **2011**, *11*, 4890−4896.

(12) Welland, M. J.; Karpeyev, D.; O'Connor, D. T.; Heinonen, O. Miscibility Gap Closure, Interface Morphology, and Phase Microstructure of 3D Li_xFePO_4 Nanoparticles from Surface Wetting and Coherency Strain. *ACS Nano* **2015**, *9*, 9757−9771.

(13) Kobayashi, G.; Nishimura, S.; Park, M.-S.; Kanno, R.; Yashima, M.; Ida, T.; Yamada, A. Isolation of Solid Solution Phases in Size-Controlled Li_xFePO_4 at Room Temperature. *Adv. Funct. Mater.* **2009**, *19*, 395−403.

(14) Wagemaker, M.; Borghols, W. J. H.; Mulder, F. M. Large Impact of Particle Size on Insertion Reactions. A Case for Anatase LixTiO2. *J. Am. Chem. Soc.* **2007**, *129*, 4323−4327.

(15) Wagemaker, M.; Mulder, F. M. Properties and Promises of Nanosized Insertion Materials for Li-Ion Batteries. *Acc. Chem. Res.* **2013**, *46*, 1206−1215.

(16) Borghols, W. J. H.; Wagemaker, M.; Lafont, U.; Kelder, E. M.; Mulder, F. M. Size Effects in the Li 4+ x Ti 5 O 12 Spinel. *J. Am. Chem. Soc.* **2009**, *131*, 17786−17792.

(17) Wagemaker, M.; Simon, D. R.; Kelder, E. M.; Schoonman, J.; Ringpfeil, C.; Haake, U.; Lützenkirchen-Hecht, D.; Frahm, R.; Mulder, F. M. A Kinetic Two-Phase and Equilibrium Solid Solution in Spinel Li4+xTi5O12. *Adv. Mater.* **2006**, *18*, 3169−3173.

(18) Okamoto, H. Supplemental Literature Review of Binary Phase Diagrams: Ag-Li, Ag-Sn, Be-Pu, C-Mn, C-Si, Ca-Li, Cd-Pu, Cr-Ti, Cr-V, Cu-Li, La-Sc, and Li-Sc. *J. Phase Equilib. Diffus.* **2017**, *38*, 70−81.

(19) Taillades, G.; Sarradin, J. Silver: High Performance Anode for Thin Film Lithium Ion Batteries. *J. Power Sources* **2004**, *125*, 199−205.

(20) Park, C.-M.; Jung, H.; Sohn, H.-J. Electrochemical Behaviors and Reaction Mechanism of Nanosilver with Lithium. *Electrochem. Solid-State Lett.* **2009**, *12*, A171.

(21) Saleh, M. S.; Li, J.; Park, J.; Panat, R. 3D Printed Hierarchically-Porous Microlattice Electrode Materials for Exceptionally High Specific Capacity and Areal Capacity Lithium Ion Batteries. *Addit. Manuf.* **2018**, *23*, 70−78.

(22) Jin, S.; Ye, Y.; Niu, Y.; Xu, Y.; Jin, H.; Wang, J.; Sun, Z.; Cao, A.; Wu, X.; Luo, Y.; Ji, H.; Wan, L.-J. Solid−Solution-Based Metal Alloy Phase for Highly Reversible Lithium Metal Anode. *J. Am. Chem. Soc.* **2020**, *142*, 8818−8826.

(23) Li, N.; Li, D.; Zhang, W.; Chang, K.; Dang, F.; Du, Y.; Seifert, H. J. Development and Application of Phase Diagrams for Li-Ion Batteries Using CALPHAD Approach. *Prog. Nat. Sci. Mater. Int.* **2019**, *29*, 265−276.

(24) Bale, C. W. W.; Bélisle, E.; Chartrand, P.; Decterov, S. A. A.; Eriksson, G.; Gheribi, A. E. E.; Hack, K.; Jung, I.-H. H.; Kang, Y.-B. B.; Melançon, J.; Pelton, A. D. D.; Petersen, S.; Robelin, C.; Sangster, J.; Spencer, P.; Van Ende, M.-A. A. FactSage Thermochemical Software and Databases, 2010−2016. *Calphad: Comput. Coupling Phase Diagrams Thermochem.* **2016**, *54*, 35−53.

(25) Gao, J.; Shi, S.-Q.; Li, H. Brief Overview of Electrochemical Potential in Lithium Ion Batteries. *Chin. Phys. B* **2016**, *25*, No. 018210.

(26) Liu, C.; Neale, Z. G.; Cao, G. Understanding Electrochemical Potentials of Cathode Materials in Rechargeable Batteries. *Mater. Today* **2016**, *19*, 109−123.

(27) Detsi, E.; Vuković, Z.; Punzhin, S.; Bronsveld, P. M. P. M.; Onck, P. R. P. R.; Hosson, J. T. M. D. J. T. M. D. Fine-Tuning the Feature Size of Nanoporous Silver. *CrystEngComm* **2012**, *14*, 5402.

(28) Deng, Z.; Detsi, E. Enhancing the Free Corrosion Dealloying Rate with a Catalytically Driven Reaction. *Nanoscale* **2017**, *9*, 11858−11863.

(29) McAlister, A. J. The Ag−Al (Silver-Aluminum) System. *Bull. Alloy Phase Diagrams* **1987**, *8*, 526−533.

(30) Ng, A. K.; Welborn, S. S.; Detsi, E. Time-Dependent Power Law Function for the Post-Dealloying Chemical Coarsening of Nanoporous Gold Derived Using Small-Angle X-Ray Scattering. *Scr. Mater.* **2022**, *206*, No. 114215.

(31) Huggins, R. A. *Advanced Batteries*; Springer US: Boston, MA, 2009.
(32) Bazant, M. 10.626 Electrochemical Energy Systems. https://ocw.mit.edu/courses/chemical-engineering/10-626-electrochemical-energy-systems-spring-2014/ Spring 2014.

https://doi.org/10.1021/acsaem.1c04127
ACS Appl. Energy Mater. 2022, 5, 4547−4555